Trans-Acting Hepatitis Delta Virus Ribozyme: Catalytic Core and Global Structure Are Dependent on the 5′ Substrate Sequence[†]

Sohee Jeong, Jana Sefcikova, Rebecca A. Tinsley, David Rueda, and Nils G. Walter*

Department of Chemistry, The University of Michigan, 930 North University, Ann Arbor, Michigan 48109-1055

Received April 21, 2003; Revised Manuscript Received May 10, 2003

ABSTRACT: The hepatitis delta virus (HDV), an infectious human pathogen affecting millions of people worldwide, leads to intensified disease symptoms, including progression to liver cirrhosis upon coinfection with its helper virus, HBV. Both the circular RNA genome of HDV and its complementary antigenome contain a common cis-cleaving catalytic RNA motif, the HDV ribozyme, which plays a crucial role in viral replication. Previously, the crystal structure of the product form of the cis-acting genomic HDV ribozyme has been determined, and the precursor form has been suggested to be structurally similar. In contrast, solution studies by fluorescence resonance energy transfer (FRET) on a trans-cleaving form of the ribozyme have shown significant global conformational changes upon catalysis, while 2-aminopurine (AP) fluorescence assays have detected concomitant local conformational changes in the catalytic core. Here, we augment these studies by using terbium(III) to probe the structure of the trans-acting HDV ribozyme at nucleotide resolution. We observe significant structural differences between the precursor and product forms, especially in the P1.1 helix and the trefoil turn in the single-stranded region connecting P4 and P2 (termed J4/2) of the catalytic core. We show, using terbium(III) footprinting and sensitized luminescence spectroscopy as well as steady-state, time-resolved, and gel-mobility FRET assays on a systematic set of substrates, that the substrate sequence immediately 5′ to the cleavage site significantly modulates these local as well as resultant global structural differences. Our results suggest a structural basis for the previously observed impact of the 5′ substrate sequence on catalytic activity.

The hepatitis delta virus (HDV)[1] ribozyme is among a class of small endonucleolytic RNAs that catalyze a reversible self-cleavage reaction that is necessary for the replication and propagation of their satellite RNA genomes. Specifically, the HDV ribozyme is a unique RNA motif found in the human hepatitis delta virus (*1*). HDV is a satellite of its helper virus, hepatitis B virus (HBV); coinfection of HDV and HBV results in intensification of the disease symptoms associated with HBV, including progression to liver cirrhosis, and affects millions of people worldwide (*2*). The small circular RNA genome of HDV replicates through a double rolling-circle mechanism, whereby multimeric units of genomic and antigenomic RNA strands are produced, followed by self-cleavage and ligation into circular monomers (*1*, *3*). Self-cleavage activity in the genomic and antigenomic RNAs resides within continuous 85-nucleotide sequences that both form a nearly identical secondary structure consisting of a nested double pseudoknot (*4*−*6*).

The genomic and antigenomic forms of the HDV ribozyme catalyze self-cleavage by a transesterification reaction, which requires deprotonation of the adjacent 2′-OH group and its nucleophilic attack on the scissile phosphate and results in formation of 2′,3′-cyclic phosphate and 5′-OH termini (*6*). The reaction mechanism of the HDV ribozyme has been extensively studied. The crystal structure of the self-cleaved product form of the genomic ribozyme reveals that a particular cytosine, C_{75} in the genomic (C_{76} in the antigenomic) ribozyme, is hydrogen bonded with the backbone of the closing loop of helix P3 and, thus, is in the proximity of the 5′-OH leaving group in the active site cleft (Figure 1) (*4*, *7*). Therefore, C_{75} has been proposed to participate directly in reaction chemistry (*4*, *7*). Subsequent kinetic studies have provided evidence that C_{75} acts either as a general base catalyst to activate the 2′-OH group as a nucleophile (*8*) or as a general acid catalyst to protonate the 5′-oxyanion leaving group (*9*−*12*). To be a reasonably effective proton acceptor or donor during catalysis at physiological pH, the pK_a of C_{75} has to be perturbed substantially from that of the free base [$pK_a \approx 4.2$ (*13*)]. Indeed, kinetic analyses have yielded estimates of ~6.1 for C_{75}'s pK_a during catalysis (*9*). Presumably, the local structure around the base, most notably, the hydrogen bond of its exocyclic amino group to the negatively charged phosphate of C_{22} observed in the crystal structure (Figure 1), provides for the electronic environment that is necessary to achieve such a significant, but not unprecedented (*14*−*16*), pK_a change. This local structure is stabilized by the essential short helix P1.1 that comprises and orients C_{22} and also buttresses the cleavage site $G_1 \cdot U_{39}$ wobble pair through stacking interactions in the tightly packed catalytic core (*5*, *17*) (Figure 1). Surprisingly, NMR-

* To whom correspondence should be addressed. Telephone: (734) 615-2060. Fax: (734) 647-4865. E-mail: nwalter@umich.edu.

[1] Abbreviations: FRET, fluorescence resonance energy transfer; fwhm, full width at half-maximum; HDV, hepatitis delta virus; NLPB, nonlinear Poisson−Boltzmann; NMR, nuclear magnetic resonance; tr-FRET, time-resolved fluorescence resonance energy transfer.
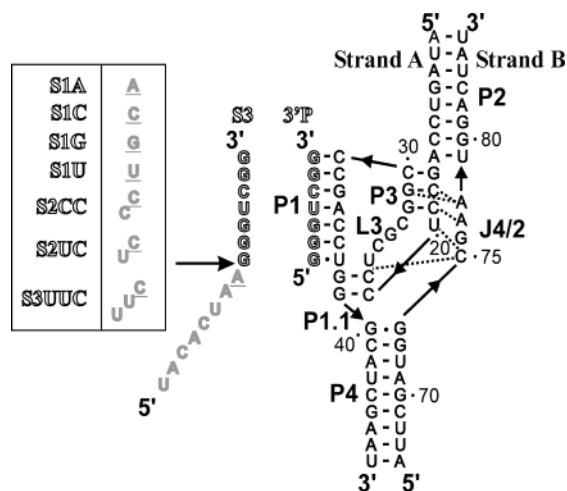
FIGURE 1: Synthetic HDV ribozyme construct D1. The ribozyme portion is shown in bold, and consists of two separate RNA strands A and B. For FRET studies, donor (fluorescein) and acceptor (tetramethylrhodamine) fluorophores were coupled to the termini of strand B (20). The 3′ product (3′P) is shown outlined. The substrate variant S3 contains eight additional nucleotides (gray) 5′ of the cleavage site (arrow). Other substrates with varying 5′ sequence as studied here are shown in the box. To generate noncleavable substrate analogues, the 2′-OH groups of the under-lined nucleotides immediately 5′ of the cleavage site were modified to 2′-methoxy groups and the suffix "nc" was added to their name. Dashed lines represent tertiary structure hydrogen bonds of C75 and the ribose zipper of A77 and A78 in joiner J4/2.

based ^{13}C chemical shift measurements found a pK_a of <5.5 for C_{75} in the product and precursor forms under all conditions that were tested, suggesting that the pK_a is only fully shifted in an intermediate state of the transesterification reaction (18).

Only a crystal structure of the self-cleaved product form of the genomic HDV ribozyme has been determined so far. On the basis of the functional importance of elements identified in this structure for the first time, such as the possible role of C_{75} in catalysis and the existence of P1.1, the assumption has been made that the precursor form of the cleavage reaction may structurally be almost identical to the product form (4). However, the product lacks the 5′ product upstream of the cleavage site (Figure 1), the sequence of which, although not base paired with the rest of the ribozyme, has been shown to have a significant impact on catalytic activity (11, 19). In fact, kinetic studies of a trans-acting HDV ribozyme have suggested that components of the substrate immediately 5′ to the cleavage site destabilize ground-state substrate binding and thereby lower the activation free energy barrier of cleavage (11). This result, in conjunction with the observation that the active site cleft in the product crystal structure is deep and tightly packed, thus not obviously providing a trajectory for substrate exit, has led to the proposal that the 5′ sequence may be accommodated by straining (bending) of the substrate and/or loosening of the catalytic core (6, 20).

Recently, we and later others have shown that trans-acting HDV ribozymes indeed undergo a conformational change upon catalysis (20−22). In particular, we have observed changes in the distance between the termini of helices P4 and P2 by fluorescence resonance energy transfer (FRET) as the precursor cleaves and the 5′ product dissociates (20). This global structural change is accompanied by a local

conformational rearrangement around C_{75}, as probed by fluorescence spectroscopy of 2-aminopurine incorporated into the neighboring position 76 (21). In addition, NMR spectroscopy has provided evidence for structural differences between the precursor and product forms of trans-acting HDV ribozymes (18, 22).

To better define these structural differences between the precursor and product forms, we now have used terbium(III)-mediated footprinting as a probe of metal binding properties as well as secondary and tertiary structure. Low (micromolar) concentrations of terbium(III), one of the lanthanide transition metal ions quite close in ion radius (0.92 vs 0.72 Å) and ligand preference to magnesium (23), displaces Mg^{2+} from only a few select sites on the RNA with the highest surface charge density. Higher (millimolar) concentrations of terbium(III) bind less specifically to RNA. Because its pK_a is close to neutrality ($pK_a = 7.9$), the aqueous Tb^{3+} complex is likely deprotonated under (near) physiological conditions, and the $Tb(OH)(aq)^{2+}$ complex cleaves the phosphodiester backbone slowly close to its location on the RNA. At low terbium(III) concentrations, this backbone scission therefore reveals high-affinity metal binding sites, while at high terbium(III) concentrations, it produces a footprinting pattern of solvent accessible regions, mainly cleaving the RNA backbone in a sequence-independent fashion (23−28). Among several metal ion-induced backbone cleavage techniques, terbium(III) has been especially favored because of its additional luminescence characteristics (23, 24, 27, 29). In particular, energy transfer from nucleobases to terbium(III) allows one to monitor the binding kinetics and thermodynamics of the lanthanide ion to the RNA (24).

Using terbium(III) luminescence spectroscopy, we now have confirmed that there are structural differences between the precursor and product forms of the trans-acting HDV ribozyme. In addition, we have used terbium(III)-mediated footprinting to reveal details of these differences at nucleotide resolution. The global structures of the precursor and product forms are similar in that they share major helices P1−P4; however, their catalytic core structures are distinct in the extent to which the short P1.1 helix forms and in the affinity of the backbone around C_{75} for metal ion binding. By systematically changing the sequence immediately 5′ to the cleavage site, we observe modulations of these differences in response to the identity and length of the 5′ sequence. These observations are supported by substantial differences in the distance of the termini of helices P4 and P2, as measured for the various ribozyme−substrate complexes by steady-state, time-resolved, and gel-mobility FRET assays. Our data are consistent with a more open catalytic core of the precursor form of the ribozyme depending on the 5′ sequence, offering a structural explanation for the impact that Been and co-workers observed for this sequence on substrate binding affinity and catalytic activity of the trans-acting HDV ribozyme (11).

MATERIALS AND METHODS

Preparation of RNA Oligonucleotides. RNA oligonucleotides were purchased with 2′ protection groups from Dharmacon Research, Inc., or from the HHMI Biopolymer/Keck Foundation Biotechnology Resource Laboratory at the Yale University School of Medicine (New Haven, CT) and were

Table 1: Kinetic and Structural Parameters of HDV Ribozyme Construct D1 in Complex with Different Substrates[a]

substrate	k_{cleav} (min^{-1})	K_M (nM)	k_{on} (M^{-1} min^{-1})	k_{off} (min^{-1})	mean D–A distance (Å)	fwhm (Å)	χ^2
S3	0.68 ± 0.08[b]	280[b]	$(7.8 \pm 0.1) \times 10^6$	0.34 ± 0.04	50 ± 1	25 ± 1	1.20
S1A	2.0 ± 0.2	59 ± 11	$(8.8 \pm 0.2) \times 10^6$	0.24 ± 0.01	56 ± 1	35 ± 1	1.19
S1G	0.19 ± 0.01	17 ± 4	$(4.2 \pm 0.4) \times 10^6$	0.20 ± 0.02	59 ± 1	34 ± 1	1.21
S1U	2.9 ± 0.3	54 ± 14	ND	ND	53 ± 1	28 ± 1	1.18
S1C	2.7 ± 0.3	69 ± 21	$(4.8 \pm 0.3) \times 10^5$	0.14 ± 0.01	54 ± 1	27 ± 1	1.22
S2CC	0.01 ± 0.005	7 ± 2	$(3.4 \pm 0.1) \times 10^6$	0.11 ± 0.01	56 ± 1	21 ± 1	1.21
S2UC	2.4 ± 0.2	71 ± 18	$(2.9 \pm 0.1) \times 10^6$	0.13 ± 0.03	56 ± 1	22 ± 1	1.17
S3UUC	1.15 ± 0.08	61 ± 12	$(3.4 \pm 0.1) \times 10^4$	0.28 ± 0.01	57 ± 1	24 ± 1	1.26
3′ P	-	-	-	-	61 ± 1	33 ± 1	1.23
none	-	-	-	-	52 ± 1	28 ± 1	1.10

[a] The cleavage rate constant k_{cleav} at substrate saturation and the apparent substrate binding constant K_M were determined as described in Materials and Methods under standard cleavage conditions: single turnover, 40 mM Tris-HCl (pH 7.5) and 11 mM MgCl$_2$ at 25 °C. k_{on} was obtained from the steady-state FRET data in Figure 6, and k_{off} upon addition of 3′P chase (see Materials and Methods), with errors derived from typically three measurements. Mean donor–acceptor distances were derived as described in Materials and Methods. fwhm is the full width at half-maximum of the distance distribution. χ^2 is the reduced χ^2 value, reporting on the quality of our data fit. ND means not determined. All parameters except for k_{cleav} and K_M were obtained using noncleavable substrate analogues. [b] Determined previously (20).

deprotected following the manufacturer's recommendations. Deprotected RNA was purified by denaturing 20% polyacrylamide, 8 M urea, gel electrophoresis, diffusion elution into 0.5 M NH$_4$OAc, 0.1% SDS, and 0.1 mM EDTA overnight at 4 °C, chloroform extraction, ethanol precipitation, and C$_8$ reverse-phase HPLC with a linear acetonitrile gradient in triethylammonium acetate as described previously (30). For FRET measurements, the three-strand ribozyme (sequences given in Figure 1) was modified on the 5′ and 3′ ends of strand B with fluorescein (donor) and tetramethylrhodamine (acceptor), respectively, as described previously (20, 30, 31). To obtain chemically blocked, noncleavable (nc) substrate analogues for structural analyses, substrates were modified with a 2′-methoxy group at the cleavage site (Figure 1). The 3′ product (3′P) has the sequence 5′-GGGUCGG-3′. RNA concentrations were calculated from their absorption at 260 nm and corrected for the additional absorption of fluorescein and tetramethylrhodamine by using the relations $A_{260}/A_{492} = 0.3$ and $A_{260}/A_{554} = 0.49$, respectively.

Handling of Terbium(III) Stock Solutions. After terbium(III) chloride [purchased from Aldrich at the highest available purity (99.9%)] had been dissolved to concentrations of 1, 10, and 100 mM in 5 mM sodium cacodylate (pH 5.5) to prevent formation of terbium(III) hydroxide precipitates at higher pH, small aliquots of these stock solutions were kept at −20 °C, as previously described (24).

Cleavage Reactions. Cleavage activities of ribozymes with different 5′ sequences were determined using the three-strand HDV ribozyme construct D1 depicted in Figure 1. The 3′ [32P]-labeled substrate was prepared by ligation with [32P]pCp using T4 RNA ligase, while the 5′ [32P]-labeled substrate was generated by phosphorylation with T4 polynucleotide kinase and [γ-[32P]]ATP, both followed by desalting using a CentriSep spin column (Princeton Separations). All cleavage reactions were conducted under single-turnover (pre-steady-state) conditions. Standard conditions were 40 mM Tris-HCl (pH 7.5) and 11 mM MgCl$_2$ at 25 °C, unless otherwise stated. Ribozyme was preannealed from strand A and twice the concentration of strand B in standard buffer, by heating to 70 °C for 2 min and cooling to room temperature over the course of 5 min. After preincubation for 15 min at 25 °C, a trace (<4 nM) amount of 3′ or 5′ [32P]-labeled substrate (for substrate S3) in standard buffer was added to a final

concentration of 10−800 nM ribozyme (based on the strand A concentration). Aliquots (5 μL) were taken at appropriate time intervals and the reactions quenched with 10 μL of 80% formamide, 0.025% xylene cyanol, 0.025% bromophenol blue, and 50 mM EDTA. The radiolabeled 3′ or 5′ cleavage product was separated from the uncleaved substrate by denaturing 20% polyacrylamide, 8 M urea, gel electrophoresis, and was quantified and normalized to the sum of the substrate and product bands using a PhosphorImager Storm 840 with ImageQuant software (Molecular Dynamics). Time traces of product formation were fit to the single-exponential first-order rate equation $y = y_0 + A_1(1 - e^{-t/\tau_1})$, employing Marquardt−Levenberg nonlinear least-squares regression (Microcal Origin), where A_1 is the amplitude and τ^{-1} the pseudo-first-order rate constant k_{obs}. Duplicates of at least four different ribozyme concentrations ([Rz]) were used to extract the catalytic rate constant k_{cleav} under standard conditions, by fitting the ribozyme concentration dependence of k_{obs} to the binding equation:

$$k_{obs} = k_{cleav} \frac{[Rz]}{[Rz] + K_M}$$

in a manner similar to the described procedures (20). K_M describes the apparent ribozyme dissociation constant for the substrate associated with catalysis and is reported in Table 1. Errors are obtained from the standard deviation of the fit parameters.

To study the inhibition of HDV ribozyme cleavage by terbium(III), separate solutions of 400 nM ribozyme and trace amounts of 5′ [32P]-labeled S3 substrate were prepared in standard buffer as described above. After preincubation for 15 min at 25 °C, varying concentrations of Tb^{3+} were added to both ribozyme and substrate. To initiate the reaction, the substrate solution was added to the ribozyme solution and reactions were quenched and analyzed as described above. The dependence of the observed cleavage rate constant on the terbium(III) concentration was fit to the following equation:

$$\text{inhibition} = (1 - k/k_0) = A_{max} \frac{[Tb^{3+}]^n}{[Tb^{3+}]^n + K_{i,app}^n}$$
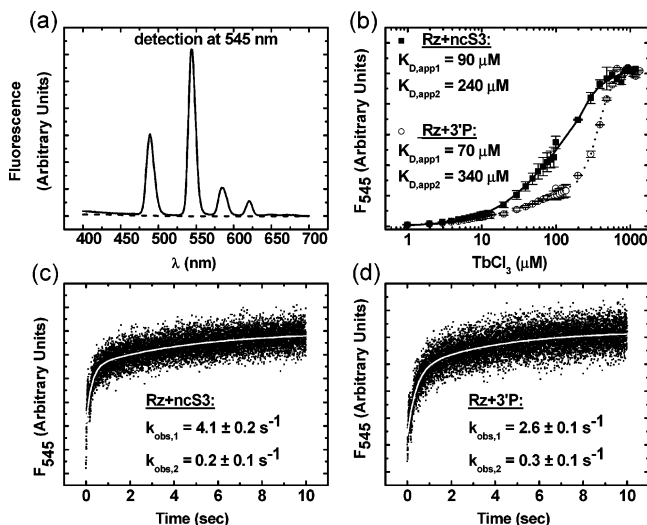
FIGURE 2: Fluorescence detection of terbium(III) binding to our trans-acting HDV ribozyme in 40 mM Tris-HCl (pH 7.5) and 11 mM MgCl$_2$ at 25 °C. (a) Characteristic emission spectrum (—) of 1 mM terbium(III) bound to 1 μM RNA upon excitation at 290 nm. In the absence of RNA, only a low background signal is observed (- - -). (b) Fluorescence titration of 1 μM HDV ribozyme complex (Rz+ncS3, precursor complex; Rz+3′P, 3′ product complex) with terbium(III). Data were fit to a sum of two independent Hill equations (lines; see Materials and Methods) to yield apparent terbium(III) dissociation constants $K_{D,app}$ as indicated. (c and d) Fluorescence signal at 545 nm over time upon mixing equal volumes of 2 mM terbium(III) with the precursor (c, Rz+ncS3) and product complexes each at 2 μM (d, Rz+3′P). Fitting to double-exponential increase functions (gray lines; see Materials and Methods) reveals two separate processes with rate constants as indicated.

where k is the cleavage rate constant in the presence of Tb^{3+}, k_0 is the cleavage rate constant in the absence of Tb^{3+}, $K_{i,app}$ is the apparent terbium(III) inhibition constant, and n is the cooperativity coefficient (*24*). Similarly, the dependence of the observed cleavage rate constant on the Mg^{2+} concentration in the presence of a constant background of 10 μM terbium(III) was fit to the following equation:

$$\text{activation} = k/k_0 = A_{\max}\frac{[\text{Mg}^{2+}]^n}{[\text{Mg}^{2+}]^n + K_{D,app}{}^n}$$

where k is the cleavage rate constant in the presence of 10 μM Tb^{3+}, k_0 is the cleavage rate constant in the absence of Tb^{3+}, $K_{D,app}$ is the apparent Mg^{2+} binding constant, and n is the cooperativity coefficient (*24*).

Terbium(III)- and Magnesium(II)-Mediated Footprinting. To observe the slow backbone scission reaction mediated by Tb(OH)(aq)$^{2+}$, purified ribozyme strands A and B were 5′ ^{32}P-phosphorylated with T4 polynucleotide kinase and [γ-^{32}P]ATP, desalted using a CentriSep spin column (Princeton Separations), and repurified by denaturing 10% polyacrylamide, 8 M urea, gel electrophoresis, followed by diffusion elution into 1 mM EDTA, and ethanol precipitation. The labeled RNA strand ($\sim$10000 dpm per 5 μL reaction volume) was preannealed with the two other unlabeled strands in standard buffer [40 mM Tris-HCl (pH 7.5) and 11 mM MgCl$_2$] by heating to 70 °C for 2 min and cooling to room temperature over the course of 5 min, followed by addition of various TbCl$_3$ concentrations (9 μM to 9 mM) and a 2 h incubation at 25 °C. Alternatively, to test the impact
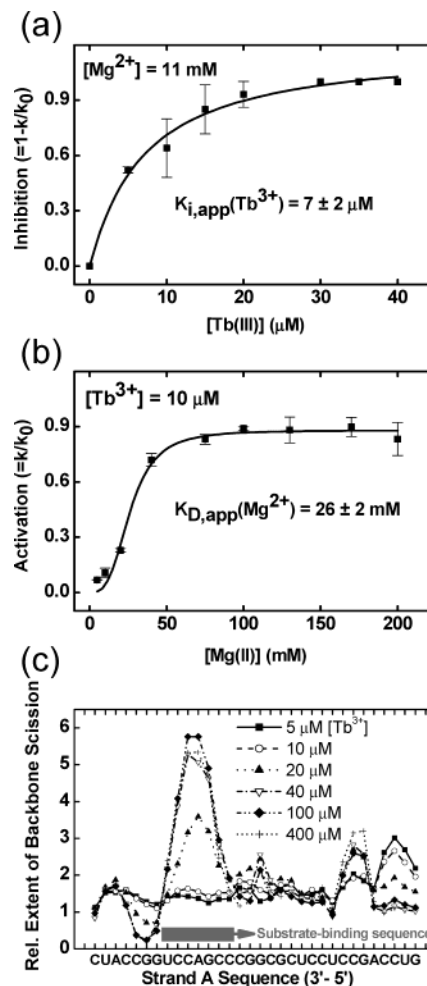

FIGURE 3: Effect of Tb^{3+} on the cleavage and binding of substrate S3 in 40 mM Tris-HCl at pH 7.5 and 25 °C. (a) Inhibition of cleavage by increasing Tb^{3+} concentrations in 11 mM Mg^{2+} background (k is the observed cleavage rate constant in the presence of Tb^{3+} and k_0 the cleavage rate constant in the absence of Tb^{3+}). Fitting to a cooperative binding (Hill) equation (—; see Materials and Methods) yields an apparent inhibition constant $K_{i,app}$ of 7 $\pm$ 2 μM (cooperativity coefficient n = 1.0) for Tb^{3+}. (b) Reactivation of cleavage by Mg^{2+} in 10 μM Tb^{3+} background. The fit to a cooperative binding (Hill) equation (—; see Materials and Methods) yields an apparent dissociation constant $K_{D,app}$ of 26 $\pm$ 2 mM (n = 3.2) for Mg^{2+}. (c) Normalized backbone cleavage induced by 3 mM terbium(III) in strand A, revealing a possible mechanism of inhibition by terbium(III) preincubation. The ribozyme−substrate complex (radiolabeled strand A, excess strand B, and noncleavable substrate analogue ncS3; see Materials and Methods) was preannealed in the presence of various micromolar terbium(III) concentrations as indicated, and then 3 mM terbium(III) was added to initiate backbone scission, probing the presence of a protecting secondary structure. With increasing terbium(III) concentrations during preincubation, the substrate binding sequence of strand A (gray bar) becomes increasingly less protected.

of preincubation with terbium(III) on substrate binding for the experiment whose results are depicted in Figure 3c, separate solutions of ribozyme (annealed from trace amounts of 5′ ^{32}P-labeled and purified strand A and a final concentration of 400 nM strand B) and noncleavable substrate analogue ncS3 (800 nM) were prepared in standard buffer supplemented with micromolar TbCl$_3$ concentrations. After preincubation for 15 min at 25 °C, the substrate and ribozyme solutions were mixed and incubated for 5 min, and 3 mM terbium(III) was added for footprinting. In all cases, the

scission reaction was stopped by addition of an equal volume of 80% formamide and 50 mM EDTA and analyzed on an 8 M urea, 20% wedged polyacrylamide sequencing gel, beside sequencing ladders from partial digestion with ribonuclease T_1 and alkali hydrolysis as described previously (23, 24). Product bands were either directly visualized using autoradiography or quantified, using a Storm 840 Phosphor-Imager with ImageQuant software (Molecular Dynamics), and normalized by calculating a relative extent of cleavage (Π) from the following equation:

$$\Pi = \frac{\left(\dfrac{\text{band intensity at nucleotide } x}{\sum_i \text{band intensity at nucleotide } i}\right)_{y[\text{Tb}^{3+}]}}{\left(\dfrac{\text{band intensity at nucleotide } x}{\sum_i \text{band intensity at nucleotide } i}\right)_{0\text{mM}[\text{Tb}^{3+}]}}$$

where y is the terbium(III) concentration in a particular cleavage reaction and x the analyzed nucleotide position of the RNA. Here, 0 mM [Tb^{3+}] signifies a control reaction mixture incubated in the same fashion as the one containing terbium(III), except that no terbium(III) is added. A Π value of ≥ 2 indicates significant cleavage over background degradation (23).

For magnesium(II)-induced scission, the RNA was prepared as described above except that 250 mM CHES-NaOH (pH 9.5) and 50 mM MgCl_2 were added instead of TbCl_3, followed by a 2 h incubation at 37 °C (32). Backbone scission was stopped, and the reaction products were analyzed as described above for terbium(III)-mediated footprinting.

Terbium(III) Luminescence Measurements. Steady-state luminescence spectra of terbium(III) bound to the preannealed and equilibrated precursor and product complexes of the HDV ribozyme (1 μM) in standard reaction buffer [40 mM Tris-HCl (pH 7.5) and 11 mM MgCl_2] at 25 °C were measured on an Aminco-Bowman Series 2 (AB2) spectrofluorometer (Thermo Spectronic), while slowly titrating TbCl_3 over several orders of magnitude from appropriate stock solutions. After each terbium(III) addition, the solution was equilibrated for 5−10 min until the signal stabilized, before an emission spectrum was recorded. Excitation was at 290 nm (slit width of 4 nm), and steady-state emission was scanned with a slit width of 8 nm. To extract the luminescence intensity of the major peak at 545 nm, each peak was fit between 535 and 555 nm with a Gaussian distribution function:

$$y = y_0 + \frac{A}{W\sqrt{\pi/2}} e^{-2[(x-x_0)^2/w^2]}$$

to yield the peak height as the pre-exponential factor, from which the background value in the absence of Tb^{3+} was subtracted. These signals were plotted over varying terbium(III) concentrations ([Tb^{3+}]) and were fit to a Hill equation (24):

$$y = y_{\max} \frac{[\text{Tb}^{3+}]^n}{[\text{Tb}^{3+}]^n + K_{\text{D,app}}{}^n}$$

to yield an apparent terbium(III) dissociation constant K_M and a cooperativity or Hill constant n. For a fit over the complete terbium(III) titration range, a sum of two independent Hill equations produced the best result, as judged by the χ^2 deviation and the residuals.

Stopped-flow kinetic experiments were performed using the Milli-Flow Reactor on the AB2 spectrofluorometer (Thermo Spectronic). A stock solution of 2 mM Tb^{3+} in standard reaction buffer was mixed with an equal volume of 2 μM preannealed precursor or product complex in standard buffer at 25 °C. Excitation was at 290 nm (slit width of 8 nm) and emission at 545 nm (slit width of 8 nm), and changes in steady-state luminescence intensity were recorded for 10 s in 1 ms time intervals. The increase in the magnitude of the signal was fit to a growth equation with two exponentials, $y = y_0 + A_1(1 - e^{-t/\tau_1}) + A_2(1 - e^{-t/\tau_2})$, and rate constants were calculated from τ^{-1} (24).

Steady-State FRET Measurements. Steady-state FRET measurements of HDV ribozyme doubly labeled with fluorescein and tetramethylrhodamine were performed on our AB2 spectrofluorometer in a manner similar to that of previously described experiments (20, 21, 30). Typically, 50 nM annealed ribozyme [final concentration; with an at least 2-fold (saturating) excess of the unlabeled strand A; lower concentrations of ribozyme were used if the substrate concentration had to be lowered; see below] was incubated at 25 °C for at least 15 min in standard buffer supplemented with 25 mM dithiothreitol as a radical quencher, and was then transferred to a 150 μL cuvette. A noncleavable substrate analogue or the 3′ product was manually added to an at least 5-fold excess to initiate the reaction, unless otherwise stated. Fluorescein was excited at 490 nm (4 nm bandwidth), and for kinetic experiments, fluorescence emission over time was recorded simultaneously at the fluorescein (520 nm, 8 nm bandwidth) and tetramethylrhodamine (585 nm, 8 nm bandwidth) wavelengths, by shifting the emission monochromator back and forth. A FRET ratio Q ($=F_{585}/F_{520}$) was calculated and normalized with its starting value to obtain the relative FRET efficiency. The resulting time traces were fit, in a manner similar to that described for the cleavage kinetics, to single-exponential increase and decrease functions of the form $y = y_0 + A_1(1 - e^{-t/\tau})$ and $y = y_0 + A_1 e^{-t/\tau}$, respectively, yielding pseudo-first-order rate constants for substrate or 3′ product binding from τ^{-1}.

To obtain bimolecular substrate binding rate constants, typically five different excess concentrations of the noncleavable substrate analogue were added. The resulting pseudo-first-order rate constants are linearly dependent on the excess concentration of substrate, indicating that the observed FRET increase is a direct result of substrate binding (20). The slope of this concentration dependence yields the second-order substrate binding rate constants k_{on} of Table 1. To obtain substrate dissociation rate constants, an at least 5-fold excess of 3′P over substrate was added to an equilibrated ribozyme−substrate complex, assembled as described above from 50 nM fluorophore-labeled strand B, 100 nM strand A, and 400 nM noncleavable substrate analogue. In each case, we observed a resultant single-exponential FRET decrease whose rate constant (derived as described above) was independent of the excess 3′P chase concentration and which therefore reflects the substrate dissociation rate constant reported in Table 1 (20).

Time-Resolved FRET Measurements. The global structures of the HDV ribozyme in complex with various substrates or the 3′ product were studied by time-resolved FRET (tr-FRET) as previously described (*20*). Preannealed complexes (75 μL; typically 0.5 μM doubly labeled ribozyme strand B, 1.0 μM strand A, and 2.5 μM either noncleavable substrate analogue or 3′ product; increasing the concentrations to 1, 3, and 6 μM, respectively, gave identical results, indicating that we are working under saturating conditions) were incubated at 25 °C for at least 15 min in standard buffer [40 mM Tris-HCl (pH 7.5) and 11 mM $MgCl_2$] supplemented with 25 mM DTT, prior to collecting time-resolved donor emission profiles using time-correlated single-photon counting, in a manner similar to previously described procedures (*20*, *21*). Briefly, a frequency-doubled Nd:YVO$_4$ laser (Spectra-Physics Millenia Xs-P, operated at 9.0 W) pumped a frequency-doubled, mode-locked Ti:sapphire laser (Spectra-Physics Tsunami, operated at 1 W) that excited fluorescein at 490 nm by 2 ps width pulses, picked down to 4 MHz. Isotropic emission was detected at 520 nm (10 nm band-pass interference filter) in 4096 sampling channels, with a time increment of 12 ps/channel, up to >40000 peak counts and under magic angle polarizer conditions. To measure donor−acceptor distances, two time-resolved fluorescence decays were collected, with and without the acceptor in place. The effect of the acceptor on the decay of fluorescein emission in the doubly labeled complex was then used to extract a three-dimensional Gaussian distance distribution between the two fluorophores as previously described in detail (*20*, *30*, *33*). In all cases, a single distance distribution gave a good fit, as judged by low reduced χ^2 values (<1.3, Table 1) and evenly distributed residuals. To calculate a mean distance, a value of 55 Å for the Förster distance R_0 of fluorescein and tetramethylrhodamine was used (*33*), assuming a value of $^2/_3$ for the orientation factor as experimentally supported by low fluorophore anisotropies (*20*).

FRET Gel Mobility Assays. FRET gel mobility assays were conducted to test the homogeneity of the various ribozyme−substrate complexes, as previously described (*20*). Nondenaturing 10% polyacrylamide (19:1 acrylamide:bisacrylamide ratio) gels containing 40 mM Tris-HCl (pH 7.5) and 11 mM Mg(OAc)$_2$ were assembled with the electrophoresis unit and equilibrated to 4 °C for at least 2 h. Doubly fluorophore-labeled ribozyme strand B (10 pmol) was annealed to strand A (20 pmol) by heating for 2 min to 70 °C and cooling to room temperature over the course of 5 min in 40 mM Tris-HCl (pH 7.5), 11 mM MgCl$_2$, 25 mM DTT, and 10% glycerol. The ribozyme was equilibrated at 25 °C for at least 15 min prior to addition of 50 pmol of substrate, noncleavable substrate analogue, or 3′ product (total volume of 20 μL). These samples were loaded on the gel, and an electric field of 8 V/cm was immediately applied. After electrophoresis for typically 20 h, the gel was scanned between its low-fluorescence glass plates in a FluorImager SI fluorescence scanner with ImageQuant software (Molecular Dynamics) as described previously (*20*, *34*). Briefly, a laser excited fluorescein at 488 nm, and the gel was scanned for fluorescence emission using a photomultiplier tube with either a 530 nm band-pass (for the donor fluorescein) or a 610 nm long-pass filter (for the acceptor tetramethylrhodamine). RNAs labeled with only fluorescein and only tetramethylrhodamine were included as color calibration

standards. From the volume reports, a measure of FRET efficiency of selected bands was calculated as $F_{acceptor}/F_{donor}$. Defining the readout of F_{donor} as green and $F_{acceptor}$ as red, we superimposed the corresponding color images using Photoshop 7.0 (Adobe) to generate Figure 7.

Electrostatic Potential Calculations. Structural coordinates of the postcleavage form of HDV ribozyme were obtained from the Protein Data Bank (PDB entry 1CX0) (*7*), and atomic radii and charges were obtained from the Amber force field. Parts of helices P1, P2, and P4 were deleted using Insight II (Accelrys Inc.) to generate a higher-resolution map of the catalytic core. Hydrogen atoms were added using the Biopolymer module of Insight II. Electrostatic potentials were calculated using the finite difference nonlinear Poisson−Boltzmann (NLPB) equation implemented in the program Delphi/Qnifft14 (*35*, *36*), and two focusing processes were performed for a higher resolution (0.94 Å/grid). Three-dimensional structures and electrostatic potentials were rendered using GRASP (*37*).

RESULTS

The Precursor and Product Forms of the Trans-Acting HDV Ribozyme Bind Terbium(III) with Different Affinities and Kinetics. Metal ion interactions are crucial for the folding and function of RNA as a polyanionic biopolymer (for a recent review, see ref *38*). Terbium(III) represents the most stable oxidation state of the lanthanide transition metal terbium. Because of their distinctive spectroscopic properties, terbium(III) and its neighbor in the periodic table, europium(III), have been extensively used to substitute for and investigate the roles of metal ions of similar size, particularly Mg^{2+} and Ca^{2+}, in protein enzymes (*39*−*41*). Although terbium has a small extinction coefficient for direct absorption, upon binding proximal to chromophores it can emit sensitized luminescence as a result of energy transfer from the chromophores. Such a case occurs when terbium(III) binds to RNA where nearby excited guanine bases transfer their energy to the lanthanide ion. Using this unique property, the metal ion binding characteristics of the hammerhead and hairpin ribozymes have recently been probed (*24*, *42*). We therefore set out to examine, by sensitized luminescence spectroscopy, the affinity and kinetics of terbium(III) binding to the precursor and product forms of our synthetic trans-acting HDV ribozyme D1 (Figure 1), which we have previously established as a suitable model system for studying the structural dynamics and function of the HDV-derived RNA enzyme (*20*, *21*).

To investigate a precursor form of construct D1, a 2′-*O*-methyl group was incorporated at the cleavage site that eliminates the nucleophilic properties of the 2′-OH group responsible for catalysis while not altering the sugar pucker preference of the ribose. Upon addition of 1 mM terbium(III) (final concentration) to 1 μM precursor HDV ribozyme (annealed from stoichiometric amounts of strands A and B and noncleavable substrate analogue ncS3; Figure 1) in standard buffer [40 mM Tris-HCl (pH 7.5) and 11 mM MgCl$_2$] at 25 °C, the emission spectrum upon excitation at 290 nm showed a terbium(III) specific signal with four peaks, the most intense of which is centered at 545 nm (Figure 2a). In the absence of RNA, no such spectrum was observed (Figure 2a). Upon terbium(III) titration, the emission at 545

nm (and proportionally those associated with the peaks at 490, 588, and 621 nm) first increased and then became saturated (Figure 2b). The resulting curve was best fit to the sum of two independent Hill equations (see Materials and Methods) (*24*), providing for two apparent dissociation constants ($K_{D,app}$) of 90 and 240 μM for dissociation from the precursor and suggesting that at least two classes of terbium(III) binding sites or modes exist. A terbium(III) titration of the 3′ product complex [1 μM; assembled from stoichiometric amounts of strands A and B and 3′P (Figure 1)] yielded two apparent dissociation constants of 70 and 340 μM (Figure 2b), again providing evidence for two classes of terbium(III) binding sites, albeit with affinities shifted compared to those of the precursor. In fact, when the precursor and product titrations are compared directly, it becomes evident that the curve for the product complex is shifted toward higher terbium(III) concentrations, suggesting weaker binding of particularly the low-affinity class of terbium(III) cations (Figure 2b).

The kinetics of terbium(III) binding can be resolved using stopped-flow experiments (*24*). To this end, we rapidly mixed terbium(III) with the preannealed HDV ribozyme complex (final concentrations 1 mM and 1 μM, respectively) under standard conditions [40 mM Tris-HCl (pH 7.5) and 11 mM MgCl$_2$ at 25 °C] and observed the sensitized luminescence at 545 nm over time. More than 30 individual stopped-flow shots were averaged, and the resulting curve was best fit to a double-exponential increase function, yielding two rate constants (Figure 2c,d). At least 66% of the fluorescence increase was associated with the faster rate constant, suggesting that terbium(III) cation binding is driven by electrostatic attraction to areas of high negative charge potential on the RNA. The precursor complex (with noncleavable substrate analogue ncS3) yielded observed rate constants of 4.1 and 0.2 s^{-1} (Figure 2c), while the product complex (with 3′P) gave values of 2.6 and 0.3 s^{-1} (Figure 2d). This suggests that the lower affinity of the product, compared to that of the precursor complex, in our terbium(III) equilibrium titration may be the result of slower terbium(III) binding kinetics.

Preincubation with Terbium(III) Results in Inhibition of Cleavage Activity. While terbium(III) is known to replace Mg^{2+} as an RNA ligand of even higher affinity, it usually inhibits catalysis by small RNA enzymes such as the hammerhead and hairpin ribozymes (*24, 29*). We therefore tested for inhibition of the HDV ribozyme by terbium(III). Cleavage reactions were performed under standard single-turnover conditions as described previously (*20*) except that varying terbium(III) concentrations (between 0 and 40 μM) were added to the separately preincubated cleavable S3 substrate and excess ribozyme solutions (Figure 1). Cleavage was initiated by mixing both solutions, followed by quantification of product formation over time to extract cleavage rate constants (see Materials and Methods). We found terbium(III) to be a potent inhibitor of catalysis by plotting the relative loss of activity, $1 - k/k_0$ [k is the rate constant in the presence of terbium(III) and k_0 the rate constant in the absence of terbium(III)], as a function of the terbium(III) concentration (Figure 3a). The resulting curve was fit to a Hill equation, yielding an apparent terbium(III) inhibition constant of 7 ± 2 μM (cooperativity coefficient $n = 1.0$) (Figure 3a). The reaction is fully inhibited at only 20 μM

terbium(III). Complementary cleavage reactions were performed with increasing Mg^{2+} concentrations (from 0 to 200 mM) in a constant background of 10 μM terbium(III). The observed rate constants increase with the Mg^{2+} concentration, and the resulting apparent dissociation constant of Mg^{2+} under these conditions is 26 ± 2 mM ($n = 3.2$) (Figure 3b). Our results suggest that binding of one terbium(III) ion at a micromolar bulk concentration can successfully compete with binding of several Mg^{2+} ions at a millimolar bulk concentration, resulting in inhibition of HDV ribozyme activity.

The mechanism of inhibition of the hammerhead and hairpin ribozymes by terbium(III) is not well understood, although it has been suggested that terbium(III), and more specifically substitution of hydrated Mg(aq)$^{2+}$ with the aqueous Tb(OH)(aq)$^{2+}$ complex, may alter the sugar—phosphate backbone geometry or flexibility or may interfere with base stacking dynamics (*24, 29*). The fact that both the hammerhead and hairpin ribozymes undergo catalysis in the presence of monovalent cations alone (*43*) rules out the notion that terbium(III) may simply inhibit by displacing a catalytically critical divalent metal ion. Likewise, the observation of residual catalytic activity of the genomic HDV ribozyme in monovalent cations alone (*9, 44*), together with the fact that no well-ordered metal ions were revealed in the crystal structure of its product form (*4, 7*), suggests that divalent metal ions do not play an absolutely obligatory role in HDV ribozyme catalysis. We therefore decided to probe further into the underlying mechanism of inhibition of our trans-acting HDV ribozyme by preincubation with terbium(III).

To this end, we used a terbium(III) footprinting assay (*23, 24*) to test whether the substrate still binds to ribozyme when both are preincubated with micromolar terbium(III) concentrations. While details of this technique are described below, it should be pointed out that in this experiment we first preincubated ribozyme and noncleavable substrate analogue ncS3 separately in the presence of micromolar terbium(III) concentrations, as was done for the cleavage assays. Then, we mixed the two RNA solutions, incubated them for an additional 5 min to allow for substrate binding, and added a high (3 mM) concentration of terbium(III) to induce backbone scission over a 2 h incubation, generating a footprint of secondary (and tertiary) structure (see also below). A quantification for ribozyme strand A is shown in Figure 3c; an increasing level of backbone scission reveals a lack of base pairing (*23, 24*). Clearly, the level of backbone scission increases specifically for the substrate-binding sequence of strand A with an increasing Tb^{3+} concentration in the preincubation buffer, indicating that the substrate no longer binds to this sequence. In fact, the Tb^{3+} concentration dependence of this destabilization of substrate binding appears to be only slightly shifted to higher concentrations (half-saturation point of ~20 μM, Figure 3c) compared to that of terbium(III) inhibition in Figure 3a ($K_{i,app} = 7$ μM). That is, the observed inhibitory effect of terbium(III) on cleavage activity of the HDV ribozyme may at least in part be due to inhibition of substrate binding. [It should be noted that inhibition of substrate binding is clearly the result of preincubation with a micromolar terbium(III) concentration rather than of footprinting with a millimolar terbium(III) concentration after assembly, as evident from the fact that no enhanced backbone scission is observed in the absence

of terbium(III) during preincubation. That is, substrate binding in the absence of terbium(III) is not reversed upon addition of terbium(III) for footprinting.] This conclusion is in contrast to the effect of terbium(III) on the catalytic activity of the hammerhead and hairpin ribozymes, where evidence from X-ray crystallography and fluorescence spectroscopy, respectively, shows that substrate is readily bound by ribozyme in the presence of inhibitory terbium(III) concentrations (*24, 29*). Our results therefore provide further evidence for a relatively low-affinity ribozyme−substrate interaction in the trans-acting HDV ribozyme (*11, 20*).

Terbium(III) Footprints HDV Ribozyme Secondary Structure at Nucleotide Resolution. High (millimolar) concentrations of terbium(III) have been used to cleave an RNA phosphodiester backbone in a largely sequence independent manner preferentially in single-stranded or non-Watson−Crick base-paired regions, thus generating a footprint of the RNA's secondary and tertiary structure at nucleotide resolution (*23−27*). In addition, because of the strongly electrostatic interaction of the highly charged Tb^{3+} with the polyanionic RNA backbone, cleavage activity is particularly enhanced on RNA surfaces of high local charge density, revealing potential metal binding sites (*23, 28, 45*). Because of its near-physiologic aqueous pK_a of 7.9 and its Mg^{2+}- and Ca^{2+}-like coordination properties with a preference for oxygen ligands, terbium(III) has recently become popular as an alternative to Mg^{2+} and Pb^{2+} ion-induced footprinting (*23*). We therefore set out to probe and compare the structures of our HDV ribozyme precursor and product complexes. To this end, trace amounts of radiolabeled strand A were preannealed with a saturating excess of unlabeled strand B and either noncleavable substrate analogue ncS3 or 3′ product (3′P) under standard buffer conditions [40 mM Tris-HCl (pH 7.5) and 11 mM $MgCl_2$ at 25 °C], followed by addition of increasing concentrations of terbium(III) to initiate slow backbone scission at 25 °C over the course of 2 h (under these conditions, only a small fraction of RNA is cleaved to avoid secondary hits on an already cut RNA molecule). Above 300 μM terbium(III), the concentration at which the RNA starts to become saturated in our equilibrium titration (Figure 2b), we observe terbium(III)-mediated backbone scission above background (Figure 4). The footprinting patterns of both the precursor (ncS3) and product (3′P) complexes are strongly biased toward the unpaired loop 3 (L3) region and the segments of helices P1 and P4 closest to P1.1. We performed similar experiments using radiolabeled strand B (data not shown), where the most intense bands appeared 3′ to the catalytic C75. A quantification of backbone scission at nucleotide resolution relative to background degradation (see Materials and Methods) is shown for the entire ribozyme in Figure 5.

The cleavage pattern of the product (3′P) complex is consistent with the crystal structure (*4*); protection is observed in all five Watson−Crick base-paired stems, P1−P4 and P1.1, while the backbone of the L3 loop region and that 3′ to C75 and G76 in the joiner between P4 and P2, called J4/2, are intensely cut (Figures 4 and 5). In contrast, the precursor (ncS3) complex is distinct; while P1−P4 remain protected, both the 5′ and 3′ segments of the P1.1 stem (as well as U20, immediately upstream) are strongly hit, suggesting that this helix is formed to a lesser extent than in the product complex (Figures 4 and 5). In addition, scission
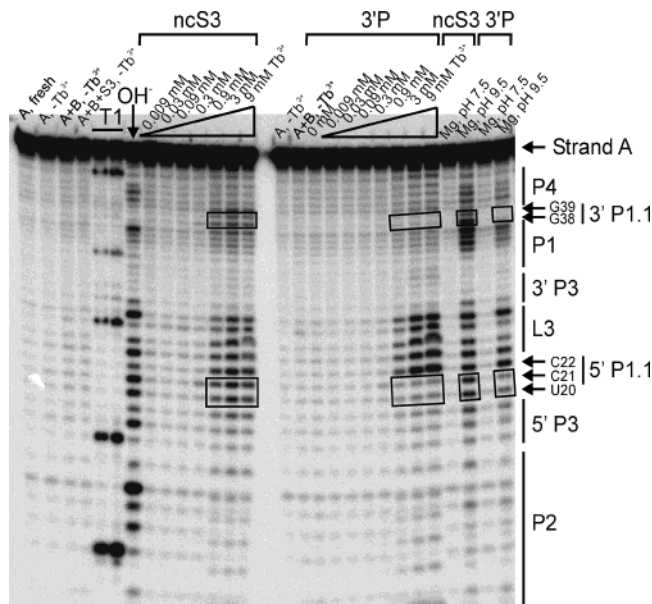

FIGURE 4: Terbium(III)- and magnesium(II)-mediated footprint of 5′ ^{32}P-labeled HDV ribozyme strand A upon incubation with terbium(III) for 2 h in 40 mM Tris-HCl (pH 7.5) and 11 mM $MgCl_2$ at 25 °C. From left to right are shown, as indicated, strand A fresh after radiolabeling, incubated in buffer without Tb^{3+}, incubated with excess strand B in buffer without Tb^{3+}, and incubated with excess strand B and noncleavable substrate analogue ncS3 in buffer without Tb^{3+}, RNase T1 digest, alkali (OH⁻) ladder, footprint with increasing Tb^{3+} concentrations in the presence of excess strand B and ncS3, incubated in buffer without Tb^{3+}, incubated with excess strand B in buffer without Tb^{3+}, and footprint with increasing Tb^{3+} concentrations in the presence of excess strand B and 3′ product (3′P). As the terbium(III) concentration is increased, backbone scission becomes more intense. The 5′ and 3′ segments of P1.1 (boxed) footprint very differently between the precursor and product complexes. At the far right is shown magnesium(II)-induced cleavage at pH 9.5 and 37 °C (see Materials and Methods); from left to right are shown the precursor (ncS3) complex incubated at pH 7.5 (control), the precursor complex footprinted at pH 9.5, the product complex incubated at pH 7.5 (control), and the product complex footprinted at pH 9.5.

in J4/2 extends to A77 and A78 (Figure 5), suggesting that the ribose zipper motif involving these nucleotides (Figure 1) may not be fully formed in the precursor complex. These results confirm that the trans-acting precursor complex undergoes a conformational change, especially in the catalytic core region of P1.1 and J4/2, upon cleavage and conversion into the product complex. While previous evidence from fluorescence resonance energy transfer (*20*), 2-aminopurine fluorescence quenching (*21*), and NMR spectroscopy (*18, 22*) have already hinted at structural differences between the precursor and product forms of the trans-acting HDV ribozyme, here we have derived specifics of these rearrangements at nucleotide resolution.

Magnesium(II) at pH 9.5 Produces a Structural Footprint Similar to That of Terbium(III). In principle, it is conceivable that the addition of 3 mM terbium(III) to the precursor (ribozyme−noncleavable substrate) complex for footprinting may specifically alter the structure of this complex so that it no longer resembles that of the product complex. To test for this possibility, we performed footprinting assays utilizing 50 mM Mg^{2+} at pH 9.5 and 37 °C instead; elevated pH and temperature produce enough deprotonated $Mg(OH)(aq)^+$ species ($pK_a = 11.4$) to act as a footprinting agent for sites of enhanced metal binding. Previously, such assays have
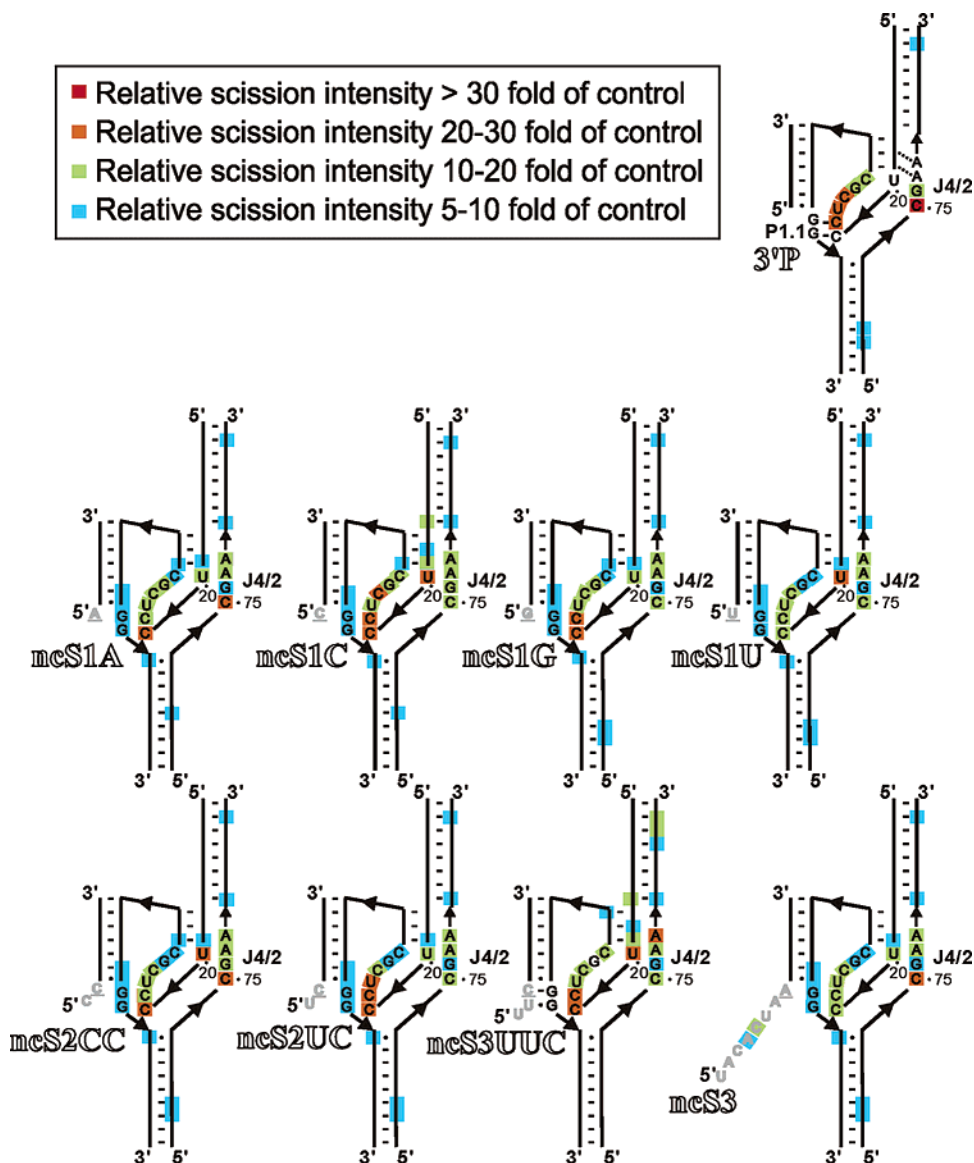
FIGURE 5: Sites of backbone scission mediated by 3 mM terbium(III) in 40 mM Tris-HCl (pH 7.5) and 11 mM MgCl₂ at 25 °C, superimposed onto two-dimensional representations of the precursor and product HDV ribozyme secondary structures. Only the catalytic core residues are explicitly shown. Relative scission intensities were calculated as described in Materials and Methods and are represented by the color code. Scission is located 3′ of the indicated nucleotides. Only the product structure is likely to fully form P1.1 and the ribose zipper of A77 and A78 in J4/2, as suggested by solid and dashed lines, respectively.

revealed a metal binding site at the bottom of the P2 stem in catalytically active HDV ribozyme—substrate complexes (*32*). We were interested in comparing the footprinting patterns in magnesium(II) and terbium(III); Figure 4 shows that they are indeed very similar. In particular, magnesium(II) footprinting reveals strongly cut 5′ and 3′ segments of the P1.1 stem in the precursor (ncS3) complex, which become highly protected in the product (3′P) complex, just as they do when using terbium(III) as the footprinting agent. These results provide further evidence for structural differences between the precursor and product complexes of the trans-acting HDV ribozyme and demonstrate the value of terbium(III) in providing unbiased information about RNA secondary and tertiary structure.

The Terbium(III) Footprinting Pattern Is Modulated by the Composition of the 5′ Substrate Sequence. The essential active site components of the HDV ribozyme are all proposed to reside in the sequence 3′ to the cleavage site since a single nucleoside 5′ to the cleavage site is sufficient for catalytic activity and does not participate in any base pairing interactions with the 3′ sequence (*46*, *47*). Nevertheless, the 5′ substrate sequence has been shown to have a significant impact on catalytic activity (*11*, *19*). Since the only difference between our precursor and product complexes is the presence of this 5′ sequence, we decided to test variations of this sequence for their impact on the observed structural differences. Guided by the catalytic studies of Been and co-workers (*11*), we chose a systematic set of substrates for our structural studies (Figure 1). First, we confirmed that the single-turnover cleavage activities of our ribozyme construct D1 vary significantly for these substrates (Table 1), generally following the trends observed by Been and co-workers [although our rate constants at 25 °C are typically 3−8-fold faster than those reported by Been at 37 °C in a similar buffer (*11*)]. Next, we performed terbium(III) footprinting assays on the noncleavable substrate analogue containing precursor complexes, and the quantified results are shown in Figure 5. All precursor complexes display
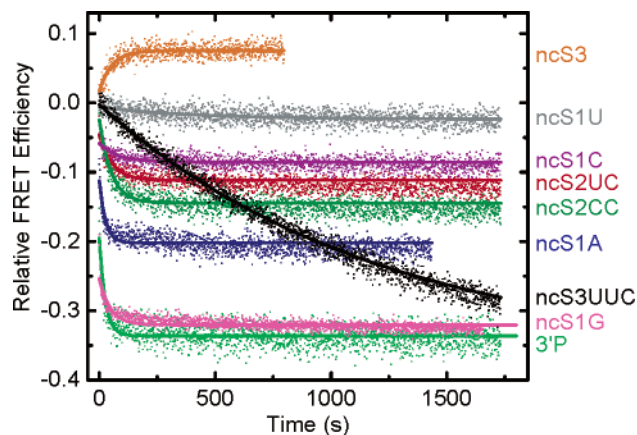
FIGURE 6: Relative steady-state FRET changes upon addition of our noncleavable substrate analogues (400 nM each) with varied 5′ sequence and of 3′ product (3′P) to 50 nM fluorescein−tetramethylrhodamine doubly labeled HDV ribozyme D1 in 40 mM Tris-HCl (pH 7.5), 11 mM MgCl$_2$, and 25 mM DTT at 25 °C. Data were fit (−) with single-exponential increase or decrease functions as required, yielding the following rate constants: 2.61 min^{-1} for ncS3, 0.14 min^{-1} for ncS1U, 0.3 min^{-1} for ncS1C, 1.05 min^{-1} for ncS2UC, 1.16 min^{-1} for ncS2CC, 3.65 min^{-1} for ncS1A, 0.05 min^{-1} for ncS3UUC, 3.1 min^{-1} for ncS1G, and 11 min^{-1} for 3′P.

cleavage patterns distinct from those of the 3′P complex, even if they only contain one additional nucleotide 5′ of the cleavage site. Consistently, the P1.1 stem and the ribose zipper motif in J4/2 are strongly cut and thus not fully formed (Figure 5). There are subtle differences among the precursor complexes; one that stands outs is that of the noncleavable substrate analogue ncS3UUC, which has the sequence UUC 5′ to the cleavage site and displays a protected 3′ and an exposed 5′ segment of P1.1, presumably due to formation of an extended substrate binding helix P1. Remarkably, noncleavable substrate analogue ncS2UC, missing only the terminal nucleotide of the 5′ sequence of ncS3UUC, does not show evidence for such a P1 extension (Figure 5).

Steady-State Fluorescence Resonance Energy Transfer (FRET) Indicates that the Differences in Catalytic Core Structure Translate into Differences in Global Structure. Previously, we have shown by steady-state FRET that binding of the noncleavable substrate analogue ncS3 by our HDV ribozyme construct D1 leads to a slight decrease in the distance (i.e., increase in FRET) between two fluorophores attached to the termini of stems P2 and P4. This observation is in contrast to the large increase in distance (decrease in FRET) resulting from binding of the 3′ product, indicative of a substantial change in global structure upon cleavage (*20*). This change is accompanied by a significant rearrangement of the catalytic core as evidenced from fluorescence dequenching of a 2-aminopurine incorporated at position 76 of the trefoil motif in the J4/2 joiner (Figure 1) (*21*). Given the variations in catalytic core structure, as probed by terbium(III) footprinting, of our precursors with systematically varied 5′ substrate sequence (Figure 5), we expected potential differences between them in our steady-state FRET assay as well. This is indeed the case; Figure 6 shows that the addition of a saturating 8-fold (400 nM) excess of each noncleavable substrate analogue to the fluorophore-labeled ribozyme leads to a FRET change of distinct rate and extent. Unlike ncS3, all shorter noncleavable substrate analogues result in a slight to significant decrease in the

extent of FRET, but not to the same extent or rate as addition of the 3′ product (3′P) that lacks the 5′ substrate sequence. The only exception is ncS1G, with only a single G 5′ to the cleavage site, whose addition to the ribozyme leads to a decrease in the extent of FRET that is nearly as large as that for the addition of 3′P (Figure 6). However, it is important to note that the corresponding cleavable S1G is a comparably poor substrate [k_{cleav} = 0.19 min^{-1}, ∼10-fold slower than most other substrates (Table 1)], suggesting that its precursor structure is not optimal for catalysis, as has been observed previously (*11*). It also should be noted that we have evidence that this particular substrate easily forms alternative, multi-meric structures, which we had to denature for all of our studies. Specifically, when we did not heat denature the noncleavable substrate analogue ncS1G prior to its addition to the FRET-labeled ribozyme, we observed only a very small decrease in the extent of FRET. In contrast, the steady-state FRET time traces of all other substrates were not altered by such heat denaturation (data not shown). Similarly, only the ncS1G substrate (and its cleavable version S1G) had to be heat-denatured prior to purification by C$_8$ reverse-phase HPLC; otherwise, a much delayed and heterogeneous elution profile compared to those of the other substrates was observed (data not shown). Presumably, this substrate, with its six guanosines out of eight nucleotides, can form more stable G-quadruplexes (*48*), which need to be denatured prior to binding to ribozyme.

By fitting our steady-state FRET data with single-exponential increase or decrease functions as required, we were able to measure the pseudo-first-order rate constants of the FRET change upon formation of the ribozyme−noncleavable substrate analogue complex for all substrates except ncS1U (which exhibited a FRET change that was too small) (Figure 6). The bimolecular substrate binding rate constants k_{on} were then extracted as described previously (*20*) from the substrate concentration dependencies of the pseudo-first-order rate constants; results are reported in Table 1. Most notably, the ncS3UUC substrate binds considerably more slowly (by 2 orders of magnitude) than nearly all other substrates. The ncS3UUC substrate also yields the most distinct terbium(III) footprinting pattern of all precursor complexes, suggesting the formation of an extended substrate binding helix P1 (see above and Figure 5). Perhaps competition with a partially formed P1.1 helix leads to the observed deceleration of substrate binding (Figure 1).

Next, we performed steady-state FRET assays in which we added a large excess of 3′P as a chase to the preformed ribozyme−noncleavable substrate analogue complex (see Materials and Methods). We have previously shown that this assay directly reports the dissociation rate constant k_{off} of the substrate (*20*), and the results of our analysis are summarized in Table 1. As expected, substrates that can have additional interactions between their 5′ sequence and the GG sequence of the 3′ segment of the P1.1 stem, such as S1C, S1CC, and S2UC (Figure 1), have slower dissociation rate constants than most other substrates [0.1 min^{-1} compared to 0.2−0.3 min^{-1} (Table 1)]. However, the S3UUC substrate again is an exception to this rule since its dissociation rate constant (0.28 min^{-1}) groups with that of the faster dissociating substrates.

Time-Resolved FRET Reveals the Global Architecture of the Precursor Complexes, while a FRET Gel Mobility Assay

Reports on Their Homogeneity. To quantify the global structural differences between the various precursor complexes and the product complex, we used time-resolved FRET (tr-FRET) to measure the distance distribution between the donor and acceptor fluorophores attached to the termini of P4 and P2, respectively, as previously described (*20*, *21*). Our tr-FRET data analysis yielded a single distance distribution for each complex that was studied, as judged by the low χ^2 values and residuals of our fits (see Materials and Methods). This confirms our result from steady-state FRET which shows there are significant differences in the global architectures of the precursor complexes, which are all distinct from the 3′ product complex (Table 1). For example, a significant increase in the mean donor−acceptor distance of 11 Å is observed upon conversion of the ncS3-containing precursor complex into the product complex, as described previously (*20*). In contrast, the slowly cleaving S1G substrate forms a precursor (ncS1G) complex with a mean donor−acceptor distance only 2 Å shorter than that of the product complex (Table 1), consistent with our steady-state FRET results (Figure 6). In general, the mean donor−acceptor distances measured by tr-FRET are consistent with the pattern of steady-state FRET changes in Figure 6, in that a smaller distance correlates with an increase in the extent of FRET and a larger distance with a decrease in the extent of FRET compared to the substrate-free ribozyme (Table 1). This demonstrates that the 5′ substrate sequence has a surprisingly significant effect on the global structure of the precursor complex, presumably resulting from the rearrangement of the catalytic core observed by terbium(III)-mediated footprinting. In addition, the full widths at half-maximum (fwhms) of the distance distributions vary significantly with the 5′ substrate sequence, perhaps indicative of changes in the overall flexibility of the complex (Table 1).

We also utilized a previously described FRET gel mobility assay (*20*, *21*) to examine the homogeneity and FRET ratios of our precursor complexes. To this end, we electrophoresed our doubly labeled HDV ribozyme construct D1 on a nondenaturing polyacrylamide gel alone and in complex with each of our noncleavable substrate analogues as well as the 3′ product (see Materials and Methods). The results of a quantitative Fluorimager analysis are shown in Figure 7. All but two precursor complexes exhibit a single band (where any alternate band contributes less than 15% of the major one), and each precursor complex shows a distinct FRET (acceptor:donor fluorescence) ratio or color in the gel. The observed colors are largely consistent with our analysis by steady-state and time-resolved FRET, in that a red-shifted gel band with respect to that of the free D1 ribozyme correlates with a steady-state increase in the extent of FRET (Figure 6) and a decrease in the donor−acceptor distance measured by tr-FRET (Table 1), while a green-shifted band correlates with a steady-state decrease in the extent of FRET and an increase in the donor−acceptor distance. However, the ability of a nondenaturing gel to separate RNA conformations on the basis of hydrodynamic radius (*49*) reveals a significant alternate conformer (band) for the precursor complexes containing the ncS1G and ncS1U noncleavable substrate analogues (having ∼56 and ∼68%, respectively, of the intensity of their major bands). In both cases, the secondary band has a lower gel mobility and is red-shifted compared to the major band (Figure 7). Interestingly, we
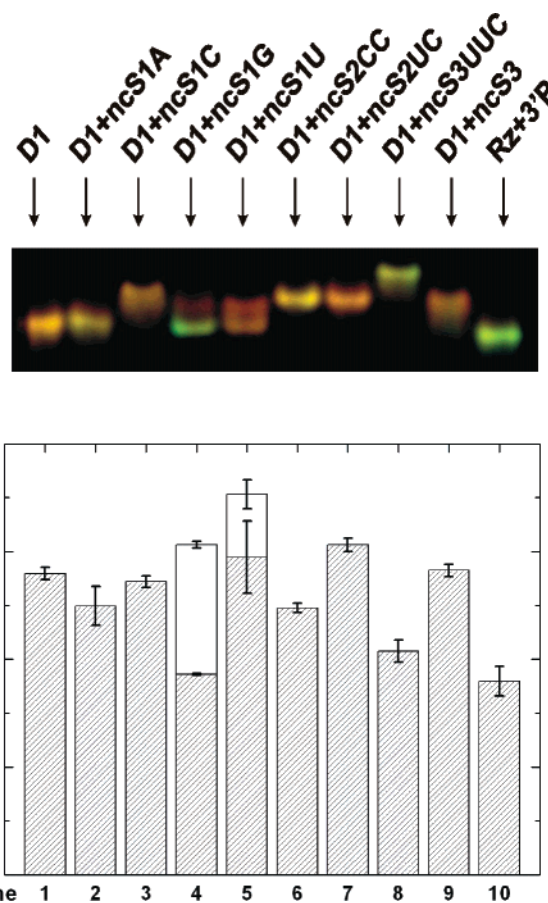

FIGURE 7: Nondenaturing gel electrophoresis of fluorescein−tetramethylrhodamine doubly labeled HDV ribozyme D1 free and in complex with our set of noncleavable substrate analogues with varying 5′ sequence and 3′ product (3′P) as indicated. The complexes exhibit not only different gel mobilities which are reflective of their hydrodynamic radii but also distinct colors and thus acceptor (tetramethylrhodamine):donor (fluorescein) ratios [bottom panel, white bars, FRET ratios of slower migrating (upper) secondary bands]. Electrophoresis and quantitative analysis were performed as described in Materials and Methods.

did not find any evidence for such defined alternate conformers in our tr-FRET analysis, where a single distance distribution in both cases gave χ^2 values of 1.21 and 1.18, respectively, comparable to those of any other complex that was studied (Table 1). It is possible that the sieving and caging effects of the polyacrylamide gel matrix or the low temperature (4 °C) during electrophoresis in these cases either slow the interconversion of existing conformers or induce novel RNA conformations that are resolved as separate bands. Nonetheless, all of our observations highlight the large influence that a single or few nucleotides of the 5′ substrate sequence, with no known interaction with the remainder of the RNA, have on the catalytic core and global structure, as well as the catalytic activity, of the HDV ribozyme.

DISCUSSION

Biological catalysis depends on the proper juxtaposition of functional groups from both the substrate and enzyme in the catalytic core of the enzyme to increase their effective concentration and lower the entropic cost of their interaction (*50*). Catalytic RNAs are no exception, as they are also believed to use this strategy to enhance their ability as enzymes (for a review, see ref *6*). As one example, the crystal

structure of the self-cleaved product of the genomic HDV ribozyme shows a tightly interwoven nested double-pseudoknot structure with five Watson–Crick base-paired stems (P1, P1.1, and P2–P4) (*4, 7*). It also reveals a trefoil turn buttressed by a downstream ribose zipper in the single-stranded region connecting P4 and P2 (J4/2), which positions the catalytic C75 into a tight catalytic core at the junction of the five stems (Figure 1). However, absent from the product crystal structure is the sequence immediately 5′ to the cleavage site, and while it is not predicted to directly base pair with any downstream elements, it must contribute to the architecture of the adjacent active site in the transition state. Consistent with this notion, the 5′ sequence has been found to strongly influence both substrate binding affinity and catalytic activity of the trans-acting HDV ribozyme (*19*); presumably, the HDV ribozyme utilizes intrinsic substrate binding energy to lower the energetic barrier of catalysis (*6, 11*). Here, we show that there is a structural basis for these observations as a systematic set of substrates leads to catalytic core structures, particularly with regard to P1.1 and J4/2, that all are substantially different from that of the product complex and where each translates into a distinct global architecture. Specifically, we have used terbium(III), which we show to bind rapidly and with two gross affinities (Figure 2), to probe the local structure of the various ribozyme–noncleavable substrate (precursor) complexes at nucleotide resolution (Figure 4). The 5′ substrate sequence subtly modulates the terbium(III) footprinting pattern, but in general, we find that P1.1 and the nucleotides involved in the ribose zipper of J4/2 only become protected in the product complex (Figure 5). The relatively subtle differences in catalytic core structure among the various precursor complexes translate into surprisingly significant changes in FRET efficiency between two fluorophores attached to the termini of P4 and P2, as evident from steady-state, time-resolved, and gel-mobility FRET assays (Figure 6, Table 1, and Figure 7, respectively). In light of such differences in HDV ribozyme precursor structure at both the local and global level, depending on the 5′ substrate sequence, it may be less surprising that their catalytic activities vary so widely (Table 1).

We find terbium(III) to be a versatile probe of HDV ribozyme secondary and tertiary structure. As detected by sensitized terbium(III) luminescence and observed before for the hairpin ribozyme, the lanthanide ion binds to the RNA with rapid, electrostatically driven, multiexponential kinetics (Figure 2c,d) and with multiple binding affinities (Figure 2b). Clearly, the ncS3-containing precursor and 3′ product complexes show distinct terbium(III) binding kinetics and affinities, consistent with their distinct local and global structures. Backbone scission with 3 mM terbium(III) at pH 7.5 over the course of 2 h at room temperature produces distinct footprinting patterns of the precursor and product secondary and tertiary structures, very similar to the patterns observed upon magnesium(II)-induced footprinting (Figure 4). Like hydroxyl radicals (*51*), terbium(III) preferentially cuts non-Watson–Crick base-paired regions which are the key to RNA function, but is simple to set up (see Materials and Methods), making it a powerful and easy-to-use structural probe. To induce backbone scission in a specific location, the aqueous $Tb(OH)(aq)^{2+}$ complex has to deprotonate the adjacent 2′-OH group which then nucleophilically
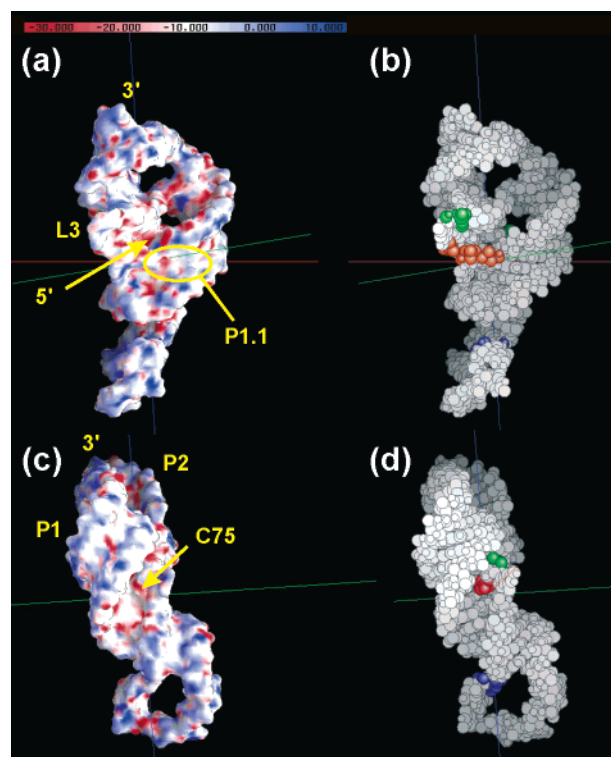

FIGURE 8: Comparison of the electrostatic surface charge potential, calculated using the NLPB equation on the crystal structure of the 3′ product form of the genomic HDV ribozyme [PDB entry 1CX0 (*7*)], with the observed backbone scission sites at 3 mM terbium(III). (a) Front view of the catalytic core. The surface charge potential is colored using the depicted scale ranging from −30 to 10 kT/e. The 5′ end is deeply buried in the catalytic pocket between P1.1 and loop L3 that is characterized by a high negative charge potential. (b) Phosphate and 2′-hydroxyl groups involved in terbium(III)-mediated backbone scission. The viewpoint is the same as in panel a, and relative scission intensities are colored as in Figure 5: red for >30-fold of control, orange for 20−30-fold of control, green for 10−20-fold of control, and blue for 5−10-fold of control. Regions close to the catalytic core, especially in loop L3, are strongly cut. (c) Surface charge potential from the back view of the molecule to highlight the joiner J4/2 that contains C75. The color code is the same as in panel a. (d) Phosphate and 2′-hydroxyl groups involved in terbium(III)-mediated backbone scission from the same viewpoint as panel c and with the color code of panel b. C75 is particularly strongly cut. All three-dimensional structures and electrostatic potentials were rendered using the program GRASP (*37*).

attacks the 3′,5′-phosphodiester bond to form 2′,3′-cyclic phosphate and 5′-hydroxyl termini. Therefore, a long residency time of the terbium(III) complex and ample access to the ribose 2′-OH group will result in a specific backbone cut (*23, 24, 27*). A long residency time of the cationic terbium(III) complex in the proximity of the polyanionic RNA backbone, in turn, depends at least in part on the electrostatic surface potential of the RNA. The crystal structure of the product form of the genomic HDV ribozyme (*4, 7*) allows us to calculate the electrostatic surface potential using the nonlinear Poisson–Boltzmann equation implemented in the program Delphi/Qnifft14 (*35, 36*) so that we can compare it with the terbium(III) scission sites in our product complex. Figure 8 shows that we indeed observe strongly hit 2′-OH and phosphodiester groups (right panels, color coded as in Figure 5), for example, in loop 3 and around C75, that coincide with a high local surface charge potential of the RNA (left panels, colored in red).

Interestingly, we confirm here our previous finding (*24*) that terbium(III) can interfere with the formation of a secondary structure element such as the substrate-binding helix P1 if added during preincubation, while it does not disrupt structures already formed (Figure 3c). In the case of the hairpin ribozyme, this observation has enabled us to study its folding pathway by order-of-addition experiments (*24*). In the case of the HDV ribozyme, it allows us to propose that the mechanism of inhibition of catalytic activity by micromolar terbium(III) concentrations (Figure 3a) is simply interference with substrate binding. However, we cannot rule out the possibility that other, more specific mechanisms are also at work, since there are slight differences in the terbium(III) dependencies of catalytic [$K_{i,app} = 7$ μM Tb^{3+} (Figure 3a)] and substrate binding inhibition [$K_{i,app}$ closer to $\sim$20 μM Tb^{3+} (Figure 3c)]. Such more specific mechanisms may include the distortion or suppression of the dynamics of essential tertiary structure elements, as suggested for the hairpin and hammerhead ribozymes (*24, 29*), or the interference with binding of a catalytically important divalent metal ion. In each case, an increase in the competing Mg^{2+} concentration is expected to recover catalytic activity, as experimentally observed (Figure 3b). The fact that we do not observe terbium(III)-mediated backbone scission at catalytically inhibiting low micromolar concentrations (Figure 4 and data not shown) does not provide evidence against the involvement of a specific terbium(III) binding site in inhibition since scission may simply not occur due to the lack of access to a nearly 2′-OH group (*23, 24, 27*).

In the absence of a high-resolution structure of the precursor of the HDV ribozyme cleavage reaction, it has not been evident whether and how the substrate sequence 5′ to the cleavage site influences the overall structure. We now have several lines of experimental evidence from terbium(III)-mediated footprinting (this work), FRET (this work and ref *20*), and 2-aminopurine fluorescence spectroscopy (*21*) that the HDV ribozyme, at least in its trans-acting form, undergoes dramatic changes in both the catalytic core and global structure upon substrate cleavage and dissociation of the 5′ sequence. It has previously been pointed out that the 5′-OH leaving group in the product crystal structure of the genomic HDV ribozyme is deeply buried within the catalytic cleft (see also Figure 8a) and that accommodation of a sequence 5′ to the cleavage site may be sterically strenuous (*6, 20, 21*). Consistent with this notion, Been and co-workers have found that in their HDV ribozyme construct the sequence components immediately 5′ to the cleavage site destabilize ground-state substrate binding. This ground-state destabilization appears to contribute up to 2 kcal/mol toward the total 8.5 kcal/mol reduction in activation free energy for RNA cleavage (*11*). It has therefore been tempting to speculate that a sharp bend in the backbone trajectory around the scissile phosphate, the energetic cost of which is expected to be dependent on the length and composition of the sequence 5′ to the cleavage site, accompanies formation of the transition state (*6, 20, 21*). According to this model, the scissile phosphate becomes positioned between helices P1 and P1.1 and exposed to the catalytic C75, which is buttressed by the J4/2 ribose zipper motif, only in the constrained transition state. Cleavage activity may therefore be controlled by the probability of access to such a transition state, which in turn is likely to be dependent on
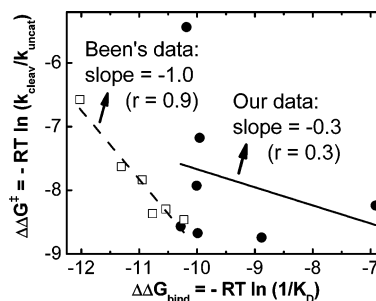

FIGURE 9: Test of a linear correlation between the substrate catalytic activation and binding free energies. The Gibbs activation ($\Delta\Delta G^{\ddagger}$) and substrate binding free energies ($\Delta\Delta G_{bind}$) were calculated as described previously (*11*) from the relations $\Delta\Delta G^{\ddagger} = -RT \ln(k_{cleav}/k_{uncat})$ and $\Delta\Delta G_{bind} = -RT \ln(1/K_D) = -RT \ln(k_{on}/k_{off})$, where R is the gas constant (1.98 cal K^{-1} mol^{-1}), T is the reaction temperature [310 K (Been's data) and 298 K (our data)], k_{uncat} is the background cleavage rate in the absence of the ribozyme (10^{-6} min^{-1}) (*11*), and k_{cleav}, k_{on}, and k_{off} are the values reported in ref *11* and Table 1 for Been's and our data, respectively: ($\square$ and $---$) Been's data (*11*) and ($\bullet$ and $-$) our data. Slopes and correlation coefficients r for the two linear fits are as indicated.

the 5′ substrate sequence, explaining our experimental observations.

We were interested in more quantitatively comparing our results with those of Been and co-workers. In particular, we wanted to test whether we find the same correlation between substrate catalytic activation and binding free energies (*11*). Our substrate dissociation and binding rate constants, k_{off} and k_{on}, respectively (Table 1), allow us to directly calculate dissociation equilibrium constants K_D from $K_D = k_{off}/k_{on}$. Surprisingly, when plotting the activation free energy ($\Delta\Delta G^{\ddagger}$) of our substrates, as calculated from k_{cleav} (Table 1), over the free energy of substrate binding ($\Delta\Delta G_{bind}$), as calculated from the dissociation equilibrium constant K_D, we observe only a very weak linear correlation (correlation coefficient $r = 0.3$) with a small negative slope (-0.3) compared to the strong linear correlation ($r = 0.9$) with a negative slope of -1 noted by Been and co-workers (Figure 9). This partial loss of correlation between destabilized ground-state substrate binding (less negative values on the x-axis of Figure 9) and reduction in activation free energy of substrate cleavage (more negative values on the y-axis of Figure 9) may have to do with the fact that the cleavage activity of our trans-acting HDV ribozyme is generally higher than that of Been's construct [with rate constants at 25 °C typically 3−8-fold faster than those reported by Been at 37 °C (*11*)]. In addition, the cleavage rate constants of our substrates are generally severalfold larger than their dissociation rate constants (Table 1), while Been's substrates follow a Briggs−Haldane type of mechanism in that their dissociation rate constants are comparable to those of cleavage. Our loss in correlation may therefore be due to a shift of our rate-limiting step away from ground-state substrate binding toward actual reaction chemistry. In that case, substrate cleavage would be expected to be faster and less determined by the binding step, as observed.

The terbium(III) footprinting patterns of our various precursor complexes give us a low-resolution picture of their ground-state structures. The enhanced access that terbium(III) generally has to the backbone of their P1.1 stem and J4/2 ribose zipper nucleotides A77 and A78 suggests that these structural elements are formed to a lesser extent than in the

product complex. A plausible notion is that these motifs form only sporadically while the precursor dynamically explores conformational space. Hence, the typical ("average") ground-state structure of the precursor may resemble the molecular model for the HDV ribozyme precursor derived by Westhof and co-workers in 1994, prior to the advent of the product crystal structure (*52*). This model predicts all four major helices (P1–P4) but lacks P1.1 and the J4/2 ribose zipper, just as suggested by our terbium(III) footprints of the precursor structure. In the event of transient formation of the key factors believed to be required for catalysis, such as P1.1, the J4/2 ribose zipper, and perhaps a substrate bend positioning the scissile phosphodiester within hydrogen bonding distance of a protonated C75, the transition state can be reached and substrate cleavage can occur. This scenario would explain why the pK_a of C75 appears to only fully shift toward neutrality in the transition state of the transesterification reaction (*18*). It may also explain the observation that catalysis by cis-acting ribozymes is generally ~10-fold faster than by trans-acting ribozymes (*6*), if we assume that their additional strand crossover between P1 and P2 (Figure 1) helps restrict the dynamics of P1 to a degree that the transition state can be reached with 10-fold higher probability. Only further experimental and modeling studies will reveal whether this prediction is correct.

ACKNOWLEDGMENT

REFERENCES

1. Lai, M. M. (1995) *Annu. Rev. Biochem. 64*, 259–286.
2. Hadziyannis, S. J. (1997) *J. Gastroenterol. Hepatol. 12*, 289–298.
3. Macnaughton, T. B., Shi, S. T., Modahl, L. E., and Lai, M. M. (2002) *J. Virol. 76*, 3920–3927.
4. Ferre-D'Amare, A. R., Zhou, K., and Doudna, J. A. (1998) *Nature 395*, 567–574.
5. Wadkins, T. S., Perrotta, A. T., Ferre-D'Amare, A. R., Doudna, J. A., and Been, M. D. (1999) *RNA 5*, 720–727.
6. Shih, I. H., and Been, M. D. (2002) *Annu. Rev. Biochem. 71*, 887–917.
7. Ferre-D'Amare, A. R., and Doudna, J. A. (2000) *J. Mol. Biol. 295*, 541–556.
8. Perrotta, A. T., Shih, I., and Been, M. D. (1999) *Science 286*, 123–126.
9. Nakano, S., Chadalavada, D. M., and Bevilacqua, P. C. (2000) *Science 287*, 1493–1497.
10. Nakano, S., and Bevilacqua, P. C. (2001) *J. Am. Chem. Soc. 123*, 11333–11334.
11. Shih, I., and Been, M. D. (2001) *EMBO J. 20*, 4884–4891.
12. Oyelere, A. K., Kardon, J. R., and Strobel, S. A. (2002) *Biochemistry 41*, 3667–3675.
13. Scheit, K. H. (1980) *Nucleotide Analogues: Synthesis and Biological Function*, John Wiley & Sons, New York.
14. Wang, C., Gao, H., Gaffney, B. L., and Jones, R. A. (1991) *J. Am. Chem. Soc. 113*, 5486–5488.
15. Legault, P., and Pardi, A. (1997) *J. Am. Chem. Soc. 119*, 6621–6628.
16. Ravindranathan, S., Butcher, S. E., and Feigon, J. (2000) *Biochemistry 39*, 16026–16032.
17. Nishikawa, F., and Nishikawa, S. (2000) *Nucleic Acids Res. 28*, 925–931.
18. Luptak, A., Ferre-D'Amare, A. R., Zhou, K., Zilm, K. W., and Doudna, J. A. (2001) *J. Am. Chem. Soc. 123*, 8447–8452.
19. Deschenes, P., Lafontaine, D. A., Charland, S., and Perreault, J. P. (2000) *Antisense Nucleic Acid Drug Dev. 10*, 53–61.
20. Pereira, M. J., Harris, D. A., Rueda, D., and Walter, N. G. (2002) *Biochemistry 41*, 730–740.
21. Harris, D. A., Rueda, D., and Walter, N. G. (2002) *Biochemistry 41*, 12051–12061.
22. Tanaka, Y., Tagaya, M., Hori, T., Sakamoto, T., Kurihara, Y., Katahira, M., and Uesugi, S. (2002) *Genes Cells 7*, 567–579.
23. Harris, D. A., and Walter, N. G. (2003) *Curr. Protocols Nucleic Acid Chem. 6.8*, Wiley, New York, in press.
24. Walter, N. G., Yang, N., and Burke, J. M. (2000) *J. Mol. Biol. 298*, 539–555.
25. Hargittai, M. R., and Musier-Forsyth, K. (2000) *RNA 6*, 1672–1680.
26. Hargittai, M. R., Mangla, A. T., Gorelick, R. J., and Musier-Forsyth, K. (2001) *J. Mol. Biol. 312*, 985–997.
27. Sigel, R. K., Vaidya, A., and Pyle, A. M. (2000) *Nat. Struct. Biol. 7*, 1111–1116.
28. Saito, H., and Suga, H. (2002) *Nucleic Acids Res. 30*, 5151–5159.
29. Feig, A. L., Scott, W. G., and Uhlenbeck, O. C. (1998) *Science 279*, 81–84.
30. Walter, N. G. (2001) *Methods 25*, 19–30.
31. Walter, N. G., and Burke, J. M. (2000) *Methods Enzymol. 317*, 409–440.
32. Lafontaine, D. A., Ananvoranich, S., and Perreault, J. P. (1999) *Nucleic Acids Res. 27*, 3236–3243.
33. Walter, N. G., Burke, J. M., and Millar, D. P. (1999) *Nat. Struct. Biol. 6*, 544–549.
34. Ramirez-Carrozzi, V. R., and Kerppola, T. K. (2001) *Methods 25*, 31–43.
35. Sharp, K. A., and Honig, B. (1990) *Annu. Rev. Biophys. Biophys. Chem. 19*, 301–332.
36. Misra, V. K., and Draper, D. E. (2000) *J. Mol. Biol. 299*, 813–825.
37. Nicholls, A., Sharp, K. A., and Honig, B. (1991) *Proteins 11*, 281–296.
38. Pyle, A. M. (2002) *J. Biol. Inorg. Chem. 7*, 679–690.
39. Horrocks, W. D., Jr. (1993) *Methods Enzymol. 226*, 495–538.
40. Frey, M. W., Frey, S. T., Horrocks, W. D., Jr., Kaboord, B. F., and Benkovic, S. J. (1996) *Chem. Biol. 3*, 393–403.
41. Dickeson, S. K., Bhattacharyya-Pakrasi, M., Mathis, N. L., Schlesinger, P. H., and Santoro, S. A. (1998) *Biochemistry 37*, 11280–11288.
42. Feig, A. L., Panek, M., Horrocks, W. D., Jr., and Uhlenbeck, O. C. (1999) *Chem. Biol. 6*, 801–810.
43. Murray, J. B., Seyhan, A. A., Walter, N. G., Burke, J. M., and Scott, W. G. (1998) *Chem. Biol. 5*, 587–595.
44. Wadkins, T. S., Shih, I., Perrotta, A. T., and Been, M. D. (2001) *J. Mol. Biol. 305*, 1045–1055.
45. Ciesiolka, J., Marciniec, T., and Krzyzosiak, W. (1989) *Eur. J. Biochem. 182*, 445–450.
46. Perrotta, A. T., and Been, M. D. (1990) *Nucleic Acids Res. 18*, 6821–6827.
47. Perrotta, A. T., and Been, M. D. (1992) *Biochemistry 31*, 16–21.
48. Hardin, C. C., Perry, A. G., and White, K. (2000) *Biopolymers 56*, 147–194.
49. Orr, J. W., Hagerman, P. J., and Williamson, J. R. (1998) *J. Mol. Biol. 275*, 453–464.
50. Fersht, A. (1999) *Structure and Mechanism in Protein Science*, Freeman, New York.
51. Brenowitz, M., Chance, M. R., Dhavan, G., and Takamoto, K. (2002) *Curr. Opin. Struct. Biol. 12*, 648–653.
52. Tanner, N. K., Schaff, S., Thill, G., Petit-Koskas, E., Crain-Denoyelle, A. M., and Westhof, E. (1994) *Curr. Biol. 4*, 488–498.